The small GTPase RAB28 is required for phagocytosis of cone outer segments by the murine retinal pigmented epithelium

Guoxin Ying[‡1], **Karsten Boldt**[§], **Marius Ueffing**[§], **Cecilia D. Gerstner**[‡], **Jeanne M. Frederick**[‡], **and Wolfgang Baehr**[‡¶||2]

From the [‡]*Department of Ophthalmology and Visual Sciences, University of Utah Health Science Center, Salt Lake City, Utah 84132, the* [§]*Institute for Ophthalmic Research, Centre for Ophthalmology, University of Tübingen, Elfriede-Aulhorn-Strasse 7, D-72076 Tübingen, Germany, and the Departments of* [¶]*Neurobiology and Anatomy and* ||*Biology, University of Utah, Salt Lake City, Utah 84112*

Edited by Henrik G. Dohlman

RAB28, a member of the RAS oncogene family, is a ubiquitous, farnesylated, small GTPase of unknown function present in photoreceptors and the retinal pigmented epithelium (RPE). Nonsense mutations of the human *RAB28* gene cause recessive cone-rod dystrophy 18 (CRD18), characterized by macular hyperpigmentation, progressive loss of visual acuity, RPE atrophy, and severely attenuated cone and rod electroretinography (ERG) responses. In an attempt to elucidate the disease-causing mechanism, we generated *Rab28*$^{-/-}$ mice by deleting exon 3 and truncating RAB28 after exon 2. We found that *Rab28*$^{-/-}$ mice recapitulate features of the human dystrophy (*i.e.* they exhibited reduced cone and rod ERG responses and progressive retina degeneration). Cones of *Rab28*$^{-/-}$ mice extended their outer segments (OSs) to the RPE apical processes and formed enlarged, balloon-like distal tips before undergoing degeneration. The visual pigment content of WT and *Rab28*$^{-/-}$ cones was comparable before the onset of degeneration. Cone phagosomes were almost absent in *Rab28*$^{-/-}$ mice, whereas rod phagosomes displayed normal levels. A protein–protein interaction screen identified several RAB28-interacting proteins, including the prenyl-binding protein phosphodiesterase 6 δ-subunit (PDE6D) and voltage-gated potassium channel subfamily J member 13 (KCNJ13) present in the RPE apical processes. Of note, the loss of PDE6D prevented delivery of RAB28 to OSs. Taken together, these findings reveal that RAB28 is required for shedding and phagocytosis of cone OS discs.

Mammalian photoreceptors renew one-tenth of the OS[3] membrane daily by adding new disc membrane at the OS base and removing senescent components distally through disc shedding and phagocytosis by the adjacent retina pigmented epithelium (1, 2). Rod outer segment (ROS) disc shedding and phagocytosis are synchronized by the circadian clock, with the peak of activity shortly after light onset (3). Mammalian cone photoreceptors undergo similar OS shedding and phagocytosis (4, 5), but peak activity varies, depending on species (5–8). Much progress has been achieved in identifying molecular components of the phagocytosis pathway, including the OS-located "eat me" signal phosphatidylserine (PS) (9), RPE membrane receptors $\alpha V\beta 5$ integrin (10) and receptor tyrosine kinase MerTK (11), and scavenger receptor CD36 (12). The vast majority of data derives from study of rodent rods, as mouse and rat retinas are ~97% rod-dominant (13).

Prenylated Rab GTPases are master regulators of membrane vesicular trafficking, and mutations in human RAB genes are associated with multiple human inherited diseases (14). Rab5 isoforms have been shown to be present in RPE phagosomes, where their function is elusive (15). Absence of geranylgeranylation at the Rab27A C terminus, caused by a defect in REP1 (Rab escort protein 1), is associated with choroideremia, a rare X-linked retina degeneration (16, 17). RAB28 is a distal member of the Rab family carrying a C-terminal CAA*X* box motif instead of the common Rab geranylgeranylation motif (18, 19) and the first Rab GTPase linked directly to human retina disease (20). Nonsense mutations in *Rab28* cause cone-rod dystrophy 18 (CRD18), presenting with foveal hyperpigmentation and atrophy, with diminished cone and rod electroretinography (ERG) responses (20–22).

Whereas the molecular basis underlying CRD18 has been obscure, our study suggests that RAB28 is an essential factor in cone-specific disc shedding and phagocytosis. In *Rab28* germ line knockout mice, which recapitulate the human CRD18 phe-

[1] To whom correspondence may be addressed: Dept. of Ophthalmology and Visual Sciences, University of Utah Health Science Center, 65 Mario Capecchi Dr., Salt Lake City, UT 84132. Tel.: 801-585-7621. E-mail: g.ying@utah.edu.

[2] Recipient of an RPB Senior Investigator award and an RPB Nelson Trust award. To whom correspondence may be addressed: Dept. of Ophthalmology and Visual Sciences, University of Utah Health Science Center, 65 Mario Capecchi Dr., Salt Lake City, UT 84132. Tel.: 801-585-6643. E-mail: wbaehr@hsc.utah.edu.

[3] The abbreviations used are: OS, outer segment; IS, inner segment; ONL, outer nuclear layer; OPL, outer plexiform layer; RPE, retinal pigmented epithelium; ROS, rod outer segment(s); COS, cone outer segment(s); PS, phosphatidylserine; GT, gene trap; GC1, guanylate cyclase 1; P, postnatal day; IP, immunoprecipitation; PNA, peanut agglutinin; LCA, Leber congenital amaurosis; ES, embryonic stem; cd, candela; ANOVA, analysis of variance; DAPI, 4′,6-diamidino-2-phenylindole; EGFP, enhanced GFP; CRD, cone-rod dystrophy; ERG, electroretinography.

notype, we found that mutant cones elongate and form enlarged tips as early as P14, suggesting a disc shedding impairment. RAB28 traffics to the photoreceptor OS in a complex with PDE6D. Further, RAB28 interacts with KCNJ13, a potassium channel in the RPE associated with Leber congenital amaurosis (LCA16); KCNJ13 may collaborate with RAB28 to facilitate COS phagocytosis.

Results

The murine Rab28 gene and splice variants

The mouse *Rab28* gene consists of nine exons and expresses three splice variants, V1–V3. The variants share amino acids 1–191 encoded by exons 1–6 but differ in their C-terminals, encoded by exons 8, 7, and 9, respectively (Fig. 1*A*). RAB28V1 (221 amino acids) and V2 (220 amino acids) carry a CAA*X* box sequence, where $X = Q$ predicts farnesylation. RAB28V3 (191 amino acids) has a shorter C-terminal region and is not prenylated. The polyclonal RAB28 antibody used in this study recognized both V1 and V2 recombinant proteins (Fig. 1*B*) and thus should also recognize V3. Recombinant variants V1 and V2 are present in the HEK293 cell body, and V2 appears to be translocated selectively into the nucleus (Fig. 1*C*).

Generation of Rab28 gene trap (GT) and knockout mice

$Rab28^{GT/GT}$ mutant mice carrying a GT cassette in intron 2 and a floxed exon 3 were generated using a EUCOMM cell line. Correct gene targeting was verified by sequencing of PCR-amplified 3′ and 5′ recombination arms and FRT and LoxP sites (Fig. 1, *D* and *E*). To avoid interference of the GT cassette on nearby gene expression, we generated a *Rab28* floxed allele ($Rab28^{fl/+}$) by crossing $Rab28^{GT/GT}$ with flippase mice; the knockout allele ($Rab28^{+/-}$) was generated subsequently by mating $Rab28^{fl/+}$ with CMV-Cre mice. $Rab28^{-/-}$ mice are viable and fertile. RAB28 protein variants of 25-kDa mobility are undetectable in $Rab28^{-/-}$ retina lysates by immunoblotting (Fig. 1*F*); variant V3 is not expressed at detectable levels in WT samples. In WT retina cryosections, RAB28 is expressed in the RPE and all photoreceptor compartments, most strongly in outer segments (Fig. 1*G*, *left*); no variant is detectable in $Rab28^{-/-}$ retina cryosections (Fig. 1*G*, *right*). When electroporated into $Rab28^{-/-}$ rods, mCherry-RAB28V2 distributes throughout the cell (Fig. 1*H*).

Rab28$^{-/-}$ mice recapitulate human CRD18

Photoreceptor function was evaluated by scotopic and photopic ERG testing over a period of 13 months. At 3 months of age, both scotopic (rod) and photopic (cone) responses are significantly reduced in $Rab28^{-/-}$ mice, with greater reduction in photopic b-wave amplitudes. Mutant scotopic a-wave amplitudes are reduced to ~70% of control (Fig. 2, *A* and *C*), whereas the photopic b-wave amplitude is <50% (Fig. 2, *B* and *D*). Retina dystrophy of human CRD18 patients is typically diagnosed in early childhood (20).

Immunolabeling of $Rab28^{-/-}$ retina with antibodies directed against guanylate cyclase 1 (GC1) or mouse cone arrestin revealed fast degeneration of cones, accompanied by progressive ROS shortening and a mild reduction of ONL thickness (Fig. 3*A*). The cone number is slightly reduced (88% of control) at 1 month (Fig. 3, *A* and *F*), but severely reduced at 3 months, and very few cones are detectable at 13 months (Fig. 3*A*, *bottom panels*). Accordingly, the scotopic a-wave amplitude declines slowly starting at 1 month, and by 13 months, it is 42% of WT controls (Fig. 3*B*). Photopic ERGs decline much faster and are attenuated at all tested time points, at 65% of control at 1 month and undetectable at 13 months (Fig. 3*C*). ONL thickness in the central retina is reduced to 87, 78, and 73% of controls by 3, 6, and 13 months of age (Fig. 3*D*), respectively, whereas mutant retina OS lengths are reduced to 69, 65, and 50% at 3, 6, and 13 months (Fig. 3*E*). Cone densities are reduced to 88, 71, 35, and 12% of control levels at 1, 3, 6, and 13 months, respectively (Fig. 3*F*).

Rab28$^{-/-}$ cones have elongated OS and enlarged OS tips

All examined rod proteins (rhodopsin, transducin, PDE6, and CNGA1) were correctly localized to the ROS of 1-month-old mutants (Fig. 4*A*, *bottom panels*). By contrast, visual pigments ML-opsin and S-opsin mislocalized in part to the IS, ONL, and OPL of mutant cones (Fig. 4 (*C* and *D*), *red arrows*). We further observed that mutant COS are elongated, stretching toward the apical RPE edge, and frequently display a bulge at the distal tip revealed by CNGA3 and cone opsin immunolabeling (Fig. 4 (*B–D*), *white arrows*). Whereas WT COS taper toward their tips (Fig. 4*F*), mutant COS exhibit enlarged, balloon-like tips carried by elongated and slender outer segments (Fig. 4, *G* and *H*). One-month-old mutant COS (21.7 ± 4.9 μm) average 43% longer than control COS (15.1 ± 1.6 μm) (Fig. 4*I*). Slight elongation of mutant COS and occasional COS tip enlargement are first observed shortly after eye opening (P12), which suggests a defect in COS membrane shedding and RPE phagocytosis (Fig. 4*E*).

A second observation gleaned from immunohistochemistry was that levels of prenylated OS proteins (G protein–coupled receptor kinase 1 (GRK1), cone PDE α-subunit (cPDEα′), and cone transducin γ-subunit (cTγ)) appear reduced in mutant cones (Fig. 5 (*A–C*), *bottom panels*). Reduction of GRK1 levels in mutant cones could be observed as early as P14 (Fig. 5*D*), whereas GRK1 levels in ROS appear comparable at both P14 and 1 month of age (Fig. 5, *A* and *D*). Western blotting using 7-week-old retina lysates showed that $Rab28^{-/-}$ COS protein levels, including cPDEα′ and GRK1, are comparable with heterozygous controls (Fig. 5, *E* and *F*). The reduction of cTγ and cPDEγ was statistically significant (Fig. 5*F*). Western blotting with 3-week-old retina lysates did not display significant differences in COS protein levels (results not shown).

Phagocytosis defects of Rab28$^{-/-}$ cones

To evaluate COS membrane shedding defects, we harvested P24 WT and mutant retinas 1.5 h after light onset and labeled fixed cryosections with combined ML- and S-opsin antibodies. At this time, cone opsin–positive phagosomes (*green*) are located within the apical RPE microvilli or RPE somata (Fig. 6*A*, *white arrows*; cone sheaths identified using peanut agglutinin (PNA; *red*)). The number of COS phagosomes is reduced in mutant retina where the COS tip enlargement is already obvious (Fig. 6*B*, *arrows*). $Rab28^{-/-}$ COS phagosome counts (Fig.

ASBMB

J. Biol. Chem. (2018) 293(45) 17546–17558 **17547**
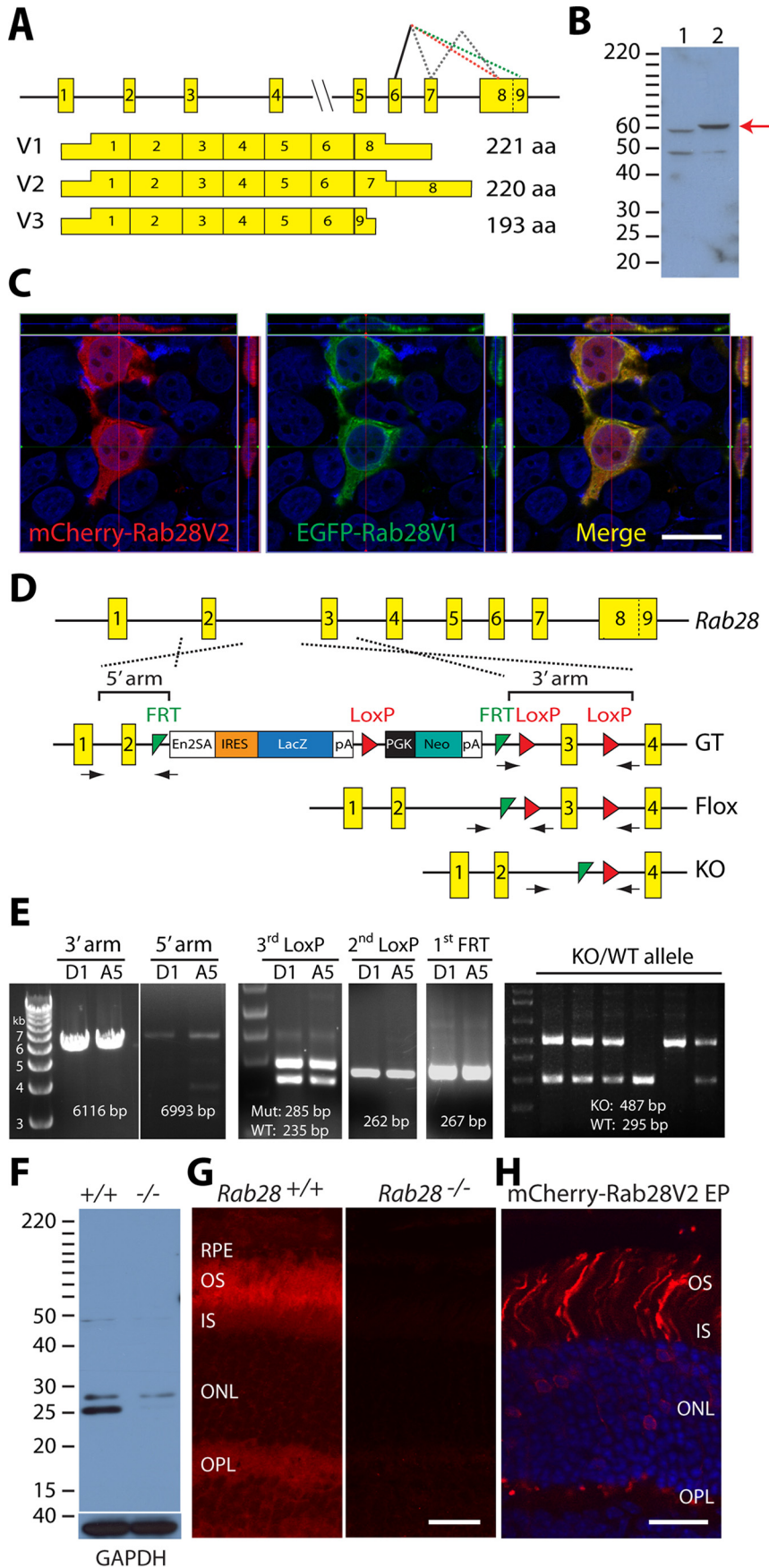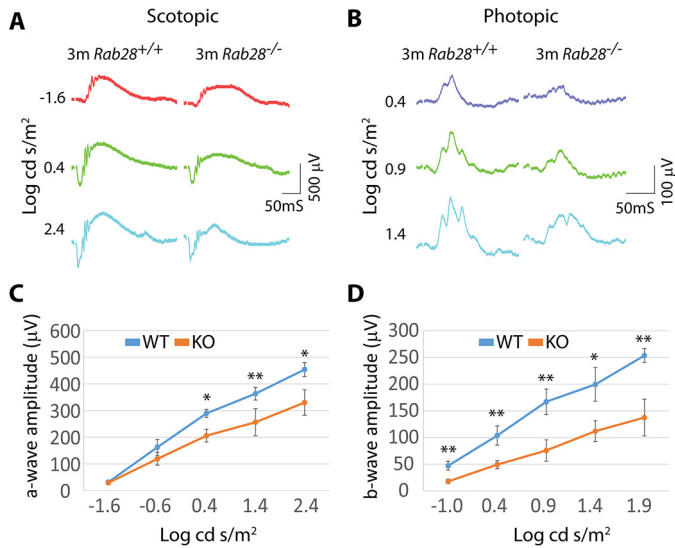
Figure 2. Reduced function of *Rab28*$^{-/-}$ photoreceptors. *A* and *B*, representative scotopic ERG (*A*) traces at −1.6, 0.4, and 2.4 log cd s/m^2 and photopic ERG traces (*B*) at 0.4, 0.9, and 1.4 photopic log cd s/m^2 from 3-month-old (*3m*) *Rab28*$^{+/+}$ and *Rab28*$^{-/-}$ mice. *C* and *D*, scotopic a-wave amplitude (*C*) and photopic b-wave amplitude (*D*) as a function of light intensity. Significant differences were observed for the scotopic a-wave amplitude at 0.4, 1.4, and 2.4 log cd s/m^2 and for the photopic b-wave amplitude at all light intensities of −0.01, 0.4, 0.9, 1.4, and 1.9 log cd s/m^2. Shown are mean ± S.D. (*error bars*), $n \geq 5$ for each group, one-way ANOVA. *, $p < 0.05$; **, $p < 0.01$; ***, $p < 0.001$.

6C) revealed a 5-fold reduction (7.5 ± 2.6 per 2-mm retina) compared with WT controls (39.8 ± 6.0 per 2-mm retina). In contrast, the rod phagosome density is comparable in P24 WT and *Rab28*$^{-/-}$ retinas (Fig. 6, *D* and *E*), by statistical evaluation, amounting to 56.3 ± 7.1 per 200-μm control RPE *versus* 51.4 ± 3.5 per 200-μm *Rab28*$^{-/-}$ RPE (Fig. 6F). These results are interpreted to indicate that *Rab28*$^{-/-}$ COS membrane shedding is defective, whereas ROS phagocytosis proceeds normally.

The *Nrl*$^{-/-}$ mouse expresses "S-cone–like" photoreceptors and is a model for enhanced S-cone syndrome in which cone phagocytosis is impaired (23). We generated *Rab28*$^{-/-}$; *Nrl*$^{-/-}$ double knockouts to analyze COS phagocytosis. We observed that *Rab28*$^{-/-}$; *Nrl*$^{-/-}$ cone tips were larger than in *Nrl*$^{-/-}$ controls (Fig. 6G, *arrows*) and that cone phagosomes could not be recorded in single (Fig. 6G) or double knockout mutants (Fig. 6H), consistent with another study (24). Larger tips in *Rab28*$^{-/-}$; *Nrl*$^{-/-}$ cones suggest a more dramatic accumulation of unshed membrane relative to *Nrl*$^{-/-}$ S-cones.

Accumulation of material in Rab28$^{-/-}$ COS tip

Transmission EM of 1-month-old *Rab28*$^{-/-}$ and heterozygous control retinas documented elongated cones with disor-
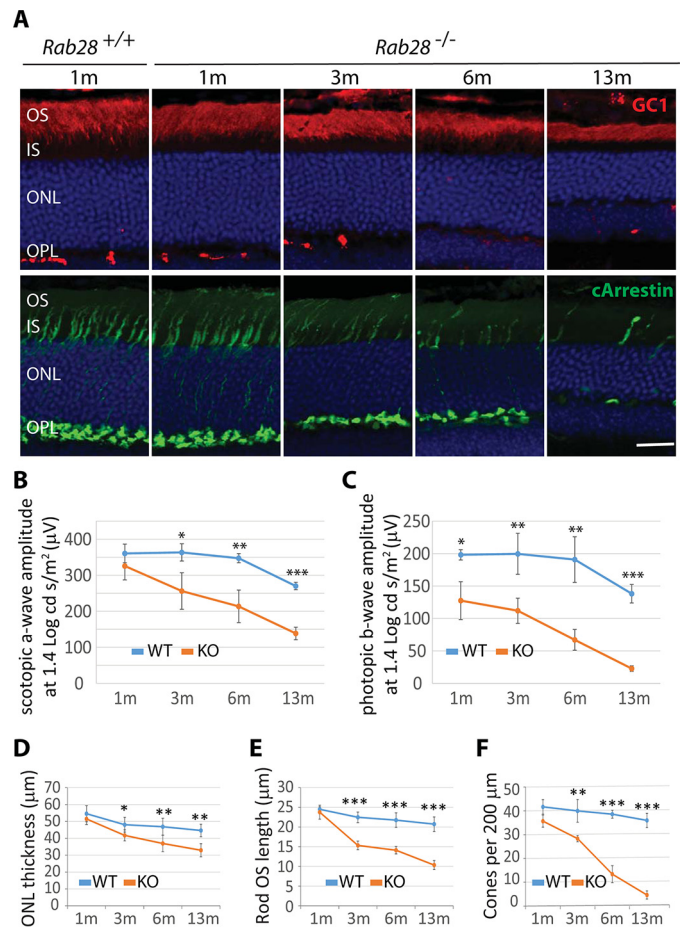
Figure 3. Progressive retina degeneration in *Rab28*$^{-/-}$ mice. *A*, immunostaining of retina frozen sections with anti-GC1 antibody (*top panels*) and with anti-cone arrestin (*bottom panels*) at 1, 3, 6, and 13 months of age. Note the gradual reduction of ROS length and ONL thickness and the more rapid cone degeneration. *Scale bar*, 20 μm. *B* and *C*, decline of scotopic a-wave (*B*) and photopic b-wave amplitudes (*C*) at 1, 3, 6, and 13 months of age. *D–F*, average ONL thickness (*D*), ROS length (*E*), and cone density (*F*) of WT and *Rab28*$^{-/-}$ retina near optic nerve at 1, 3, 6, and 13 months of age. All are significantly reduced at 3, 6, and 13 months. Shown are mean ± S.D. (*error bars*), $n = 4$, one-way ANOVA. *, $p < 0.05$; **, $p < 0.01$; ***, $p < 0.001$.

ganized distal membranes in mutants (Fig. 7, *A* and *B*). At the *Rab28*$^{-/-}$ RPE/photoreceptor interface, we observed RPE microvilli-wrapped structures filled with distorted membrane stacks or vacuolar membranes (Fig. 7, *C* and *D*). These structures appear in different shapes (round and oblique) at least 2 μm in size (Fig. 7, *F* and *G*), indicating buildup of materials at the OS tip. The size of the vacuoles (Fig. 7 (*F* and *G*), *yellow arrows*) and the shapes of membrane stacks (Fig. 7 (*F* and *G*),

Figure 1. Generation of *Rab28*$^{-/-}$ mice. *A*, *schematic representation* of the mouse *Rab28* gene and three splice variants, V1–V3. The mouse *Rab28* gene consists of nine exons (*yellow rectangles*). *Dashed gray*, *red*, and *green lines* indicate three types of mRNA splicing. V1, V2, and V3 share exons 1–6 but differ in the C terminus, which is encoded by exons 8, 7, and 9, respectively. *aa*, amino acids. *B*, Western blotting of HEK293 lysates expressing mCherry-RAB28V2 (*lane 1*) and EGFP-RAB28V1 (*lane 2*). The polyclonal antibody used in this study recognizes both variants (*red arrow*); the faster moving polypeptide is nonspecific. *C*, mCherry-RAB28V2 and EGFP-RAB28V1 expression pattern in HEK293 cells. V1 and V2 colocalize in the cytoplasm, and V2 is also present in the nucleus. *Top* and *right small panels*, orthogonal views of *y* and *z* planes at the *lines* indicated. *Scale bar*, 20 μm. *D*, *schematic representation* of the *Rab28* gene, the location of the gene trap in intron 2, the floxed allele, and the knockout allele. The En2SA-IRES-LacZ-pGK-Neo GT cassette is flanked by two FRT sites (*green triangle*) and is inserted into intron 2 by homologous recombination. Exon 3 is flanked by two LoxP sites (*red triangle*). *Small arrows* represent the approximate position of primers for genotyping. *E*, PCR genotyping of the 3′ and 5′ recombination arm, third LoxP, second FRT/LoxP, and first FRT sites in ES cells. *D1* and *A5*, two ES cell clones and the derived mice with identical genotyping results. The *right-most panel* represents a PCR genotyping result of one litter of *Rab28*$^{+/-}$ × *Rab28*$^{+/-}$ pups. Primer sequences are listed in Table S1. *F*, retinal lysate Western blotting. *Left lane*, RAB28 with a mobility of 25 kDa; *right lane*, RAB28 is absent in *Rab28*$^{-/-}$ retina lysate. The identity of the slower moving species is unknown. *G*, immunohistochemistry of WT (*left*) and knockout retina cryosections (*right*) with anti-RAB28 antibody. RAB28 is present in WT photoreceptors and RPE and absent in *Rab28*$^{-/-}$ sections (*right*). *H*, expression of mCherry-RAB28V2 in rod photoreceptors by neonatal electroporation. *Scale bars*, 20 μm. GAPDH, glyceraldehyde-3-phosphate dehydrogenase.
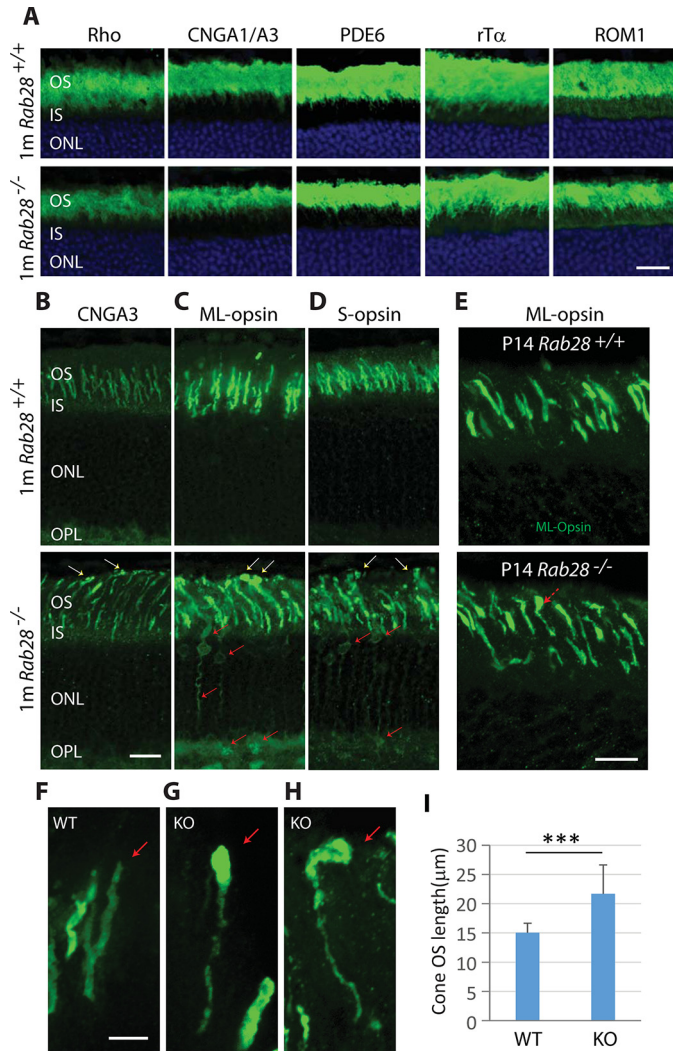
Figure 4. Cone outer segment elongation and tip enlargement in *Rab28*$^{-/-}$ retina. *A*, immunohistochemistry of 1-month-old WT (*top panels*) and *Rab28*$^{-/-}$ (*bottom panels*) retina frozen sections with antibodies against rhodopsin, CNGA1/A3, PDE6, rod Tα, and ROM1, as indicated. The immunostaining showed correct localization of ROS proteins in *Rab28*$^{-/-}$ rod photoreceptors. *B–D*, immunostaining of 1-month-old WT (*top panels*) and *Rab28*$^{-/-}$ (*bottom panels*) retina sections with anti-CNGA3 (*B*), ML-opsin (*C*), and S-opsin (*D*). *White arrows* point to the bulged COS tips at the apical RPE (*B–D, bottom panels*). *Red arrows*, cone opsin mislocalization in the IS, ONL, and OPL (*C* and *D, bottom panels*). *E*, ML-opsin staining of P14 WT (*top*) and *Rab28*$^{-/-}$ (*bottom*) retina sections. Mutant COS are slightly elongated, and enlarged COS tips are occasionally observed (*dashed arrow* in *E*). *F–H*, high-magnification confocal images of two WT COS (*F*) and two mutant COS (*G* and *H*). WT COS taper toward the RPE, but mutant COS have a balloon-like enlargement at the distal tip (*red arrows*). *Scale bars*, 20 μm (*A–D*), 10 μm (*E*), and 5 μm (*F–H*). *I*, average length of 1-month-old mutant COS (21.7 ± 4.9 μm) is significantly longer than seen in WT COS (15.1 ± 1.6 μm). Shown are mean ± S.D. (*error bars*). More than 80 cones from four animals were measured; one-way ANOVA. ***, $p < 0.001$.

arrowheads) within these bulbous structures also vary. As these structures correspond to the bulges of COS tips seen in *Rab28*$^{-/-}$ immunostaining (Fig. 4), the variable-size vacuoles and distorted membranes stacks may represent different stages of COS degeneration. Additionally, there are increased RPE pigment deposits in *Rab28*$^{-/-}$ compared with *Rab28*$^{+/-}$ controls (Fig. 7 (*C* and *D*), *dashed arrows*). By contrast, ROS disc morphology appears to be normal in *Rab28*$^{-/-}$ rods (Fig. 7*H*).

RAB28 interacts with KCNJ13, an RPE microvillus protein

Co-immunoprecipitation (co-IP) using bovine retina lysates followed by MS was performed to identify interacting proteins. We identified dozens of potential interactors (*t* test, $p < 0.05$, RAB28 IP/control IP ratio >3, Table S2). Top candidates include the prenyl-binding protein PDE6D, which has been reported previously to interact with RAB28 (25). Three other notable candidates are KCNJ13, mutations of which are associated with Leber congenital amaurosis (LCA16) (26); MEF2D, a transcription factor required for photoreceptor development and maintenance (27); and GLUT1 (glucose transporter 1), mediating RdCVF (rod-derived cone viability factor)-induced cone survival (28). In selective Western blotting verification, we successfully verified the interaction of RAB28 with KCNJ13, MEF2D, GLUT1, VAC14, and PDE6D, but failed to validate GRK1 and CAND1 (Fig. 8*A*), indicating high reliability of our co-IP results.

KCNJ13 is located at the root of WT apical RPE microvilli (29) and overlaps with the cone sheath marker, PNA (Fig. 8*B*). This pattern is preserved in *Rab28*$^{-/-}$ (Fig. 8*C*). Because the possible alteration of KCNJ13 localization on cone-associated microvilli could be masked by the overwhelming signal of rod-associated microvilli, we determined the KCNJ13 localization in *Rab28*$^{-/-}$; *Nrl*$^{-/-}$ mice. KCNJ13 is located at the RPE microvilli that span the entire short OS in *Nrl*$^{-/-}$ control animals (Fig. 8*D*). However, in *Rab28*$^{-/-}$; *Nrl*$^{-/-}$ double knockout mice, KCNJ13 is partially trapped at the base of apical RPE microvilli (Fig. 8*E*), suggesting a role of RAB28 in KCNJ13 microvilli trafficking.

RAB28 is PDE cargo targeted for the OS

To elucidate the nature of PDE6D–RAB28 interaction, we co-expressed PDE6D-EGFP and mCherry-RAB28V2 in HEK293 cells and repeated co-immunoprecipitation using mCherry antibody. As expected, mCherry-RAB28V2 co-precipitated PDE6D-EGFP (Fig. 9*A*). However, mCherry-RAB28V2-C217A, in which the cysteine of the CAA*X* box motif is mutated to alanine, preventing farnesylation, is unable to interact with PDE6D-EGFP, indicating that the interaction is RAB28 prenylation-dependent (Fig. 9*A*). Nonfarnesylated mCherry-Rab29V2-C217A distributed evenly within the cell due to the loss of membrane association (Fig. 9*B*). In *PDE6d*$^{-/-}$ mice, RAB28 is absent in the OS but accumulates in the IS (Fig. 9*C*), verifying that RAB28 is a PDE6D cargo, as observed for other prenylated OS proteins (30). The PDE6D level is unchanged in *Rab28*$^{-/-}$ retina (Fig. 9*D*).

Discussion

RAB28 has been suggested to participate in lysosomal delivery of endocytosed surface protein in unicellular trypanosomes (31), angiotensin-induced NF-κB nuclear delivery and activation in rat endothelia (32), glucose transporter 4 plasma membrane trafficking in mouse skeletal muscle (33), and intraflagellar transport in *Caenorhabditis elegans* (34).

In this study, we show that *Rab28* germ line knockout mice recapitulate the human CRD18 phenotype. In human CRD patients, the *RAB28* gene carries nonsense mutations in exons 5 and 6, truncating all known splice variants (20). CRD may be
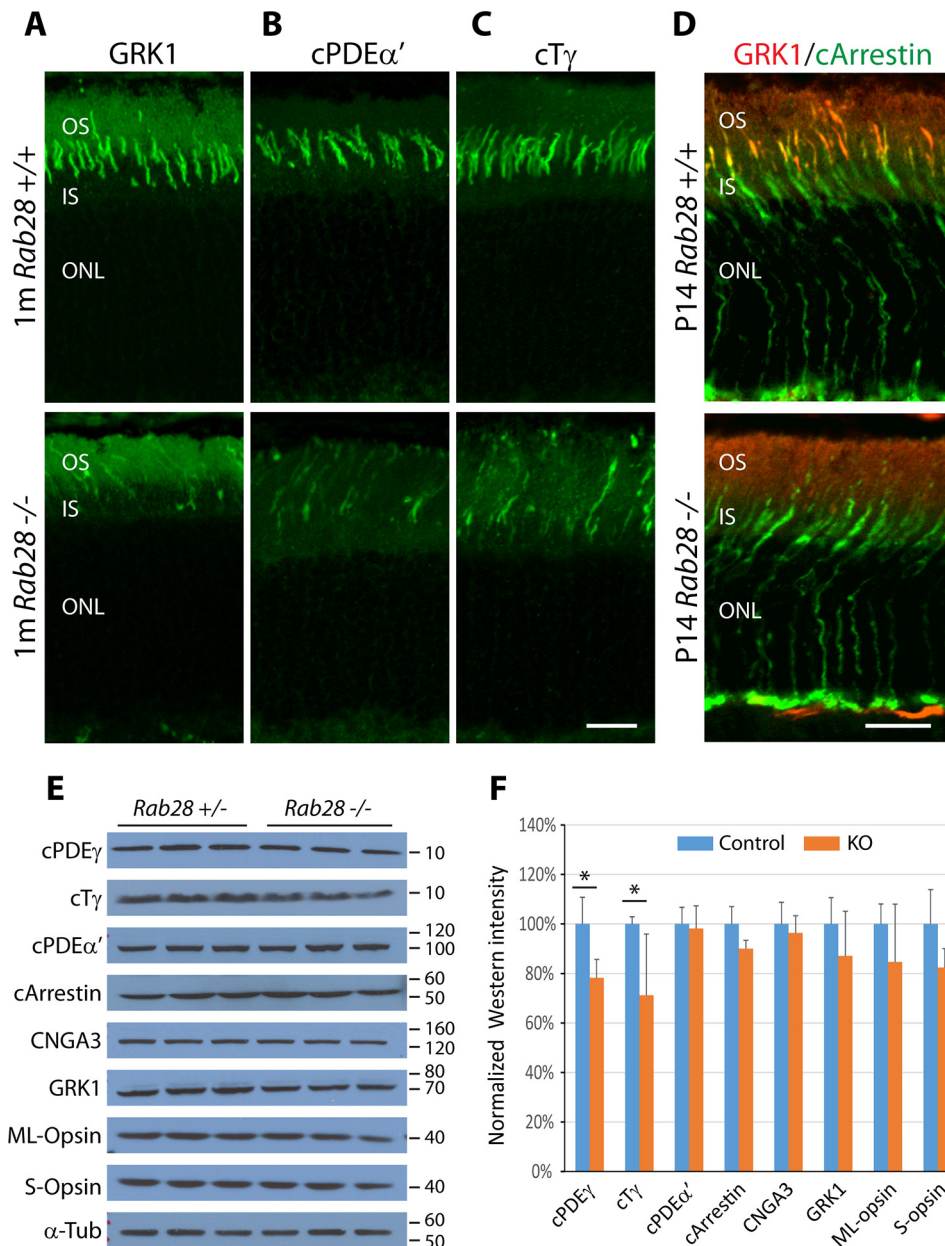
Figure 5. Reduction of prenylated protein levels in *Rab28*$^{-/-}$ cone OS. *A–C*, immunostaining of WT and GRK1 (*A*), cPDEα′ (*B*), and cTγ (*C*) in 1-month WT (*top*) and *Rab28*$^{-/-}$ (*bottom*) retinas. All three cone OS prenylated proteins showed a reduction in intensity in *Rab28*$^{-/-}$ compared with WT, whereas GRK1 in rod OS is not reduced. *D*, GRK1 (*red*) and cone arrestin (*green*) staining in P14 WT (*top*) and *Rab28*$^{-/-}$ (*bottom*) retina. GRK1 reduction in cone OS is already obvious at this stage. *Scale bars*, 20 μm. *E*, Western blotting of 7-week-old *Rab28*$^{+/-}$ and *Rab28*$^{-/-}$ retina lysate with anti-cPDEγ, anti-cTγ, anti-cPDEα′, anti-cArrestin, anti-CNGA3, anti-GRK1, and anti-M- and S-opsin antibodies. α-Tubulin was used as loading control. *F*, quantification of Western blotting signal intensity (mean ± S.D. (*error bars*)), normalized to α-tubulin. Only the reduction of cPDEγ and cTγ is statistically significant. *, $p < 0.05$, $n = 3$, one-way ANOVA.

accompanied by visual acuity deterioration, absence of photopic ERG responses, and myopia as early as age 16. In the *Rab28*$^{-/-}$ mouse model, photopic b-waves are reduced at 1 month and nearly absent by 1 year of age, which is roughly consistent with human CRD (Figs. 2 and 3).

We found that *Rab28*$^{-/-}$ COS are elongated to the length of rod outer segments, and the mutant tips are expanded to balloon-like structures and appear unable to shed membranes to be phagocytosed by the RPE. In view of impaired disc shedding at the distal cone outer segment, continued overproduction of new disc membranes at the proximal end may provide a jammed gate impenetrable for prenylated proteins (see the model in Fig. 10). The absence of membrane shedding is supported by dramatic reduction of cone pigment–containing phagosomes (Fig. 6). Bulbous OS tips and lack of phagosome production was also observed in the *Nrl*$^{-/-}$ mouse, a model for enhanced S-cone syndrome (24). *Rab28*$^{-/-}$ COS elongation and enlarged COS tips were observed shortly after eye opening (Fig. 4). We propose that CRD18 is caused by impaired membrane shedding at the distal COS and/or failed phagocytosis by the RPE. The resulting accumulation is detrimental for cone survival. The molecular identities of components involved in human and mouse disc shedding are currently unclear. Human cone membrane shedding, observed *in vivo* by adaptive optics
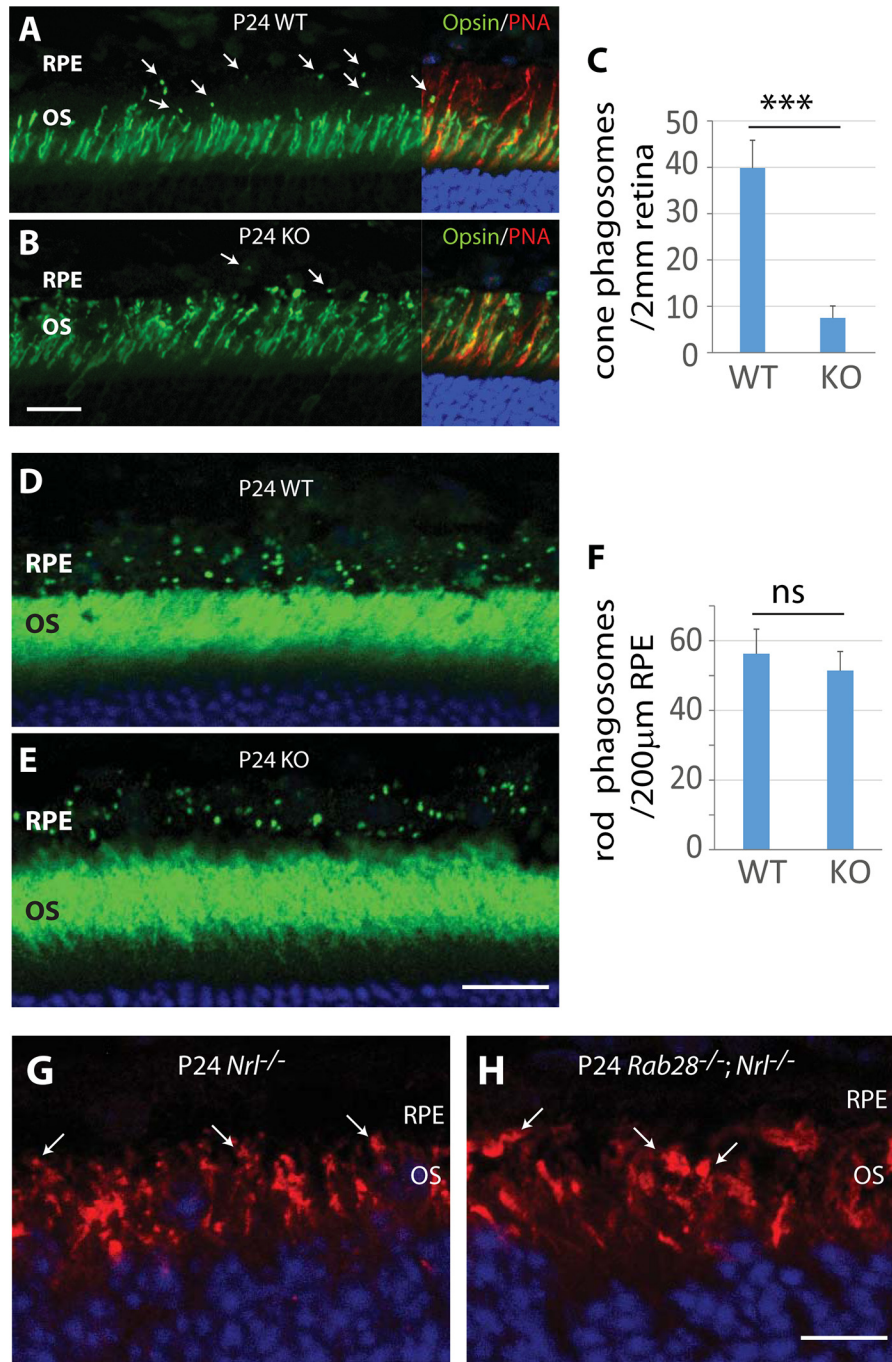
Figure 6. Reduced COS phagosomes in P24 *Rab28*⁻/⁻ retina. *A* and *B*, immunohistochemistry of P24 WT (*A*) and *Rab28*⁻/⁻ (*B*) retina cryosections with anti-ML- and anti-S-opsin antibodies (mixed 1:1) (*green*). Retina samples were collected at 1.5 h after light onset. Cone opsin-positive COS phagosomes (*arrows*) in mutant (*bottom*) were diminished compared with WT control (*top*). At the *right* of each *panel* is an overlay with PNA (*red*) and the nuclear marker, DAPI (*blue*). *C*, quantitative evaluation of COS phagosomes at P24. Mutant COS phagosome count is significantly reduced compared with WT (*Rab28*⁻/⁻ 7.5 ± 2.6 *versus* WT 39.8 ± 6.0 per 2-mm retina). Phagosomes of 12 sections from three animals (four sections for each retina) were counted. Shown are mean ± S.D. (*error bars*), one-way ANOVA. ***, $p < 0.001$. *D* and *E*, rhodopsin immunostaining of 1-month WT (*D*) and *Rab28*⁻/⁻ (*E*) retina sections collected 1.5 h after light onset. Both the density and size of rhodopsin-positive phagosomes (*green dots* at RPE) are comparable between WT and *Rab28*⁻/⁻. *F*, quantitative evaluation of ROS phagosomes at P24. Mutant ROS phagosomes are comparable with WT (*Rab28*⁻/⁻ 51.4 ± 5.5 *versus* WT 56.3 ± 7.1 per 200-μm RPE). Phagosomes of 12 sections from three animals (four sections for each retina) were counted. *ns*, not significant. *G* and *H*, S-opsin immunostaining of P24 *Nrl*⁻/⁻ (*G*) and *Rab28*⁻/⁻;*Nrl*⁻/⁻ (*H*) retina sections collected at 1.5 h after light onset. S-opsin-positive phagosomes are barely detected in the RPE of both genotypes. However, the OS tips are larger in *Rab28*⁻/⁻;*Nrl*⁻/⁻ cones compared with *Nrl*⁻/⁻ cones (*arrows*). *Scale bars*, 20 μm (*A*, *B*, *D*, and *E*) and 10 μm (*G* and *H*).

optical coherence tomography (8), was characterized by abrupt and transient loss of the COS tip. Average duration of tip loss was ~9 min, and average length loss was reported as 2.1 μm.

In 1-month-old *Rab28*⁻/⁻ retina, COS are elongated, and COS distal tips are filled with vacuoles and/or distorted mem-branes (Fig. 7). The accumulated membranes resemble material observed in degenerating *Nrl*⁻/⁻ mouse cones at 8 weeks of age (24). We did not detect organized COS discs in the enlarged *Rab28*⁻/⁻ tips similar to those observed in 4-week *Nrl*⁻/⁻ ret-ina (24), indicating that *Rab28*⁻/⁻ COS degeneration starts ear-
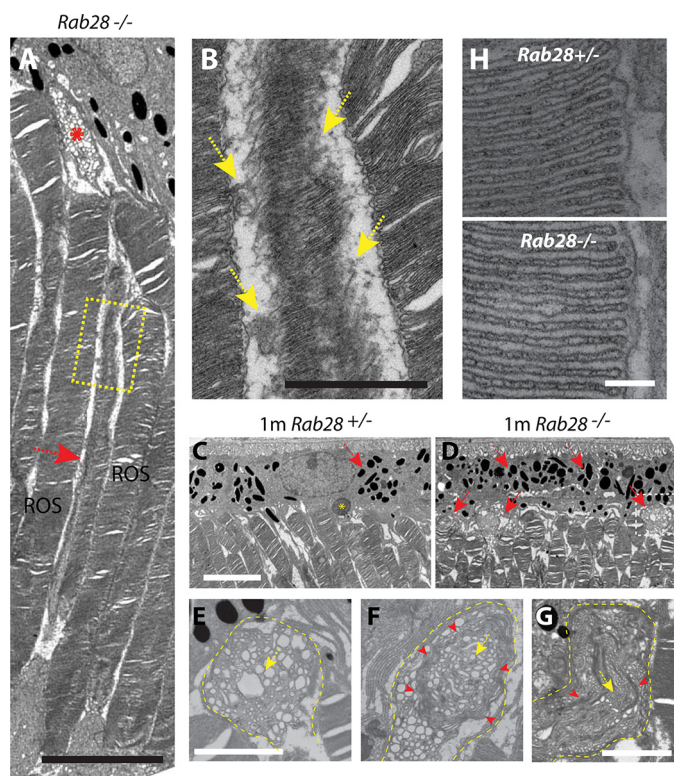
Figure 7. Ultrastructure. *A*, longitudinal image of 1-month-old *Rab28*$^{-/-}$ outer segments, showing an elongated COS (*arrow*) wedged between two ROS and reaching the apical RPE. A swollen, degenerating COS tip (*red asterisk*), belonging to the same cone, is membrane-bound and filled with vacuoles. *B*, enlargement of *yellow boxed area* in *A*, showing the partially disorganized distal COS (*yellow arrows*). *C* and *D*, representative electron micrographs of 1-month-old (*1m*) *Rab28*$^{+/-}$ (*C*) and *Rab28*$^{-/-}$ retinas (*D*). The asterisk in *C* marks a normal phagosome. *Arrows* in *D* indicate three enlarged mutant COS tips filled with membrane stacks or vacuoles at the RPE/photoreceptor interface. Note the increased pigment density in the mutant RPE (*arrows*). *E*–*H*, magnified images of three enlarged tips, ~2 μm in the shortest dimension, in mutants with variable-size vacuoles (*dashed arrows*) and distorted membranes (*arrowheads*). *Scale bars*, 5 μm (*A*), 1 μm (*B*), 5 μm (*C* and *D*), 2 μm (*E*–*G*), and 100 nm (*H*).

lier and is more severe. Another notable observation is that both *Rab28*$^{-/-}$ and *Nrl*$^{-/-}$ showed COS disorganization at the disc periphery. The *Rab28*$^{-/-}$ disc edge shows merger/swelling or disassembly (Fig. 7*B*), whereas the *Nrl*$^{-/-}$ disc edge reveals interconnection (24), suggesting that the COS disc edge is vulnerable to the accumulation of oxidative materials.

Bulbous *Rab28*$^{-/-}$ OS tips are only observed in mutant cones, as mutant rods are initially unaffected and shed discs exhibit a normal phagosome count (Fig. 6). The reason for this specificity is unknown. ROS phagocytosis is triggered by diurnal surface exposure of the anionic phospholipid phosphatidylserine at the OS tip (9), which is recognized by multiple RPE membrane receptors and their ligands, including integrin αVβ5 and ligand MFG-E8 (10, 35), MerTK and ligand proteins S and Gas6 (11, 36–38), and CD36, which directly binds PS (12). Following substrate–receptor binding, the shed ROS tip is engulfed and ingested by the RPE apical microvillus. MerTK signaling plays a critical role in initiating this process (11). Whether COS phagocytosis is subjected to similar molecular regulation is unknown. Phagocytosis requires that internalized COS phagosomes move along the microvillus before entering the RPE soma (39). However, as both αVβ5 integrin and CD36

localize at the RPE soma (10, 12), their participation in COS recognition and binding is unlikely. A recent large-cohort genetic study of inherited retina diseases found that MerTK mutations exist in a small percentage of CRD patients (40), suggesting a conserved MerTK-dependent mechanism between ROS and COS phagocytosis. In agreement with this, MerTK is expressed at apical RPE microvilli (38). As RPE signals actively participate in delineating the position of disc shedding (*e.g.* the localized PS exposure) at ROS tips (9), the failed *Rab28*$^{-/-}$ shedding phenotype may indicate a communication defect between RPE microvilli and mutant COS tips.

Our protein–protein interaction screen identified the RPE microvilli–resident protein, KCNJ13, as a RAB28 interactant. Recessive mutations of *KCNJ13* are associated with LCA16 in humans, with an undefined mechanism (26). *Kcnj13* mutant mice generated with the CRISPR-Cas9 system showed mosaic expression of KCNJ13 in RPE cells and photoreceptor degeneration resembling LCA (41). RPE cells null for KCNJ13 can survive, but KCNJ13 expression is required for RPE cells to maintain photoreceptor survival (41). We found that KCNJ13 delivery to RPE microvilli in *Rab28*$^{-/-}$; *Nrl*$^{-/-}$ double knockout is partially reduced (Fig. 8), providing a clue that RPE phagocytosis may be impaired as well. We speculate that absence of RAB28 may alter the KCNJ13 activity, which in turn affects the function of RPE microvilli and cone phagocytosis.

A second important RAB28 interactant is PDE6D, a prenylbinding protein. A *Pde6d*$^{-/-}$ mouse develops recessive CRD in which prenylated OS proteins (cPDEα', GRK1) are absent in the COS (30). We showed previously that RAB28 trafficking to the ROS is ARL3-GTP– dependent (42). Our finding that farnesylated RAB28 is unable to traffic to the OS in the absence of PDE6D (Fig. 9*C*) raises the interesting point that the cone-rod dystrophy in *PDE6d* mutant mice may result partly from the absence of RAB28 in cones. A PDE6D null allele in human patients was associated with Joubert syndrome and shown to impair trafficking of INPP5E, a phosphatidylinositol polyphosphate phosphatase involved in phosphatidylinositol metabolism (43).

The *Rab28*$^{-/-}$ mouse model provides evidence that CRD18 is caused by a defect in cone disc shedding. Owing to continuous renewal of membranes containing phototransduction components at the proximal OS and the absence of disc shedding, mutant OSs stretch toward the RPE and expand their tips to a balloon-like structure. Cone pigment– containing phagosomes are dramatically reduced. However, because RPE and cones collaborate in phagocytosis and RAB28 is normally expressed in the RPE, a role of the *Rab28*$^{-/-}$ in defective RPE phagocytosis cannot be excluded.

Experimental procedures

Animals

Animal procedures were approved by the University of Utah institutional animal care and use committee and were conducted in compliance with the National Institutes of Health Guide for Care and Use of Laboratory Animals.
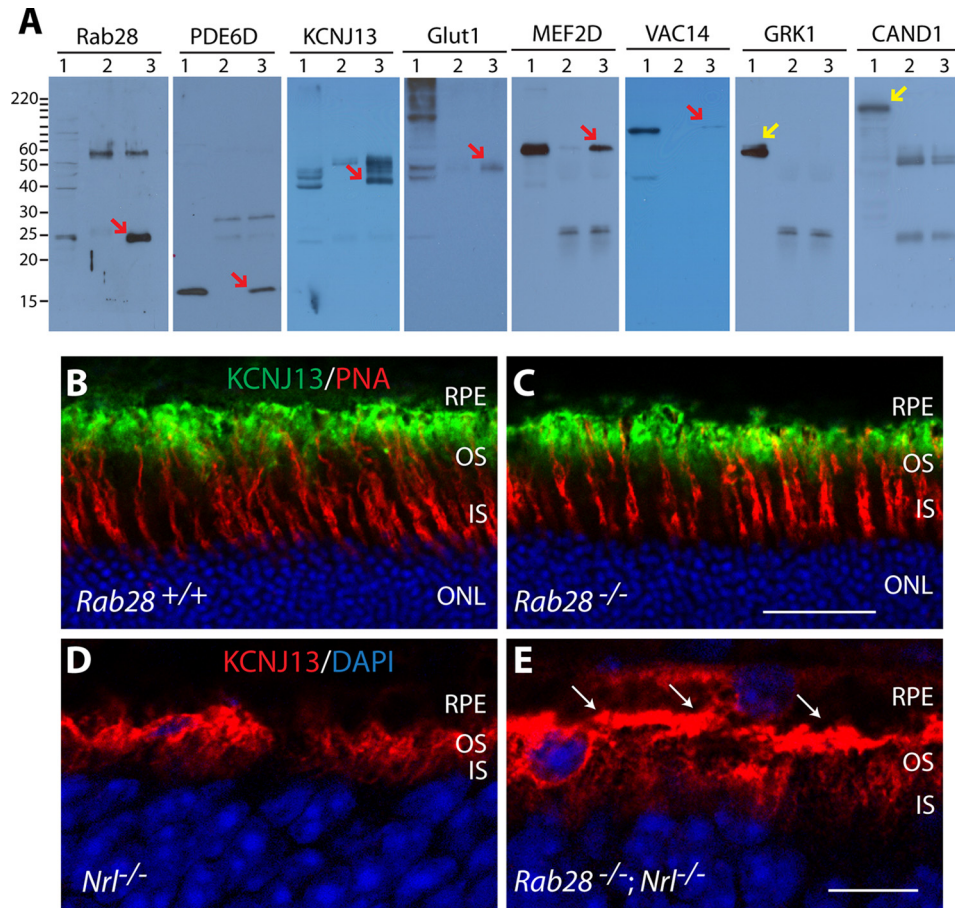
Figure 8. Rab28-interacting proteins. *A*, immunoblot verification of co-IP (Table S2) between RAB28 and select candidate proteins. Verified interactants include PDE6D, KCNJ13, MEF2D, GLUT1, and VAC14. GRK1 and CAND1 failed verification. *Lane 1*, input; *lane 2*, normal goat IgG control IP; *lane 3*, RAB28 antibody IP. Correctly verified proteins (*red arrows*) and two proteins that failed verification (*yellow arrows*) are indicated. *B* and *C*, representative immunohistochemistry using anti-KCNJ13 antibody (*green*) and PNA (*red*) in P24 WT (*B*) and *Rab28*$^{-/-}$ (*C*) retinas. KCNJ13 localization at RPE apical microvilli is comparable between WT and *Rab28*$^{-/-}$. *D* and *E*, immunohistochemistry with anti-KCNJ13 antibody (*red*) to show relative delivery of KCNJ13 in P21 *Nrl*$^{-/-}$ (*D*) and *Rab28*$^{-/-}$; *Nrl*$^{-/-}$ (*E*) double-knockout retinas/RPE. KCNJ13 is partially trapped at the base of RPE apical microvilli in double-knockout mice (*arrows* in *E*). *Scale bars*, 20 μm (*B* and *C*) and 10 μm (*C* and *D*).

Generation of Rab28$^{-/-}$ mouse

Rab28 embryonic stem (ES) cells (clones EPD0688_3_D01 and HEPD0677_7_A05), in C57BL/6N genetic background, JM8A3.N1 subline) containing a gene trap in intron 2 were acquired from EUCOMM (Helmholtz Zentrum, Munich, Germany). ES cell blastocyst injection, generation of chimera, and generation/breeding of heterozygous (GT/+) mice were performed at the University of Utah transgenic core. The *rd8* mutation (44) was removed by crossing our *Rab28*$^{GT/+}$ animals with C57BL/J WT mice. We crossed *Rab28*$^{GT/GT}$ with flippase mice (C57BL/6 background) to generate animals with a floxed allele (*Rab28*$^{fl/+}$) (Fig. 1D). Exon 3 was deleted by crossing *Rab28*$^{fl/fl}$ with CMV-Cre mice (C57BL/6 background) to generate *Rab28*$^{+/-}$ and *Rab28*$^{-/-}$ mice. Mice were maintained under 12-h cyclic dark/light conditions. ES cell and mouse tail genomic DNA was extracted using a standard protocol (45). Routine genotyping was performed using genomic DNA prepared with HotSHOT (46). PCR genotyping primers and other primers (see below) are listed in Table S1.

RNA extraction, RT-PCR, and plasmid construction

Retina tissues were dissected from WT mice, and total RNA was extracted using TRIzol reagent (Invitrogen). Reverse tran-

scription was performed using SuperScript II reverse transcriptase (with random primers) following the manufacturer's instructions. Full-length RAB28V1 and RAB28V2 were amplified by PCR and cloned into pEGFP-C1 and pmCherry-C1 (Clontech), respectively. PDE6D-EGFP was kindly provided by Dr. Houbin Zhang (University of Electronic Science and Technology of China, Chengdu). Nonprenylated RAB28V2-C217A was generated using the Phusion site-directed mutagenesis kit (Thermo Fisher Scientific). All plasmids were verified by Sanger sequencing.

ERG

ERG was performed on 1-, 3-, 6-, and 13-month-old *Rab28*$^{-/-}$ and WT control animals ($n = 5$ each group) using an UTAS E-3000 universal electrophysiological system (LKC Technologies) as described (47). Briefly, mice were dark-adapted overnight, anesthetized by intraperitoneal injection of ketamine (100 μg/g body weight) and xylazine (10 μg/g body weight) in 0.1 M PBS, and loaded onto a recording platform with body temperature maintained at 37 $\pm$ 0.5 °C. After dilating pupils with 1% tropicamide solution (Bausch & Lomb Inc., Tampa, FL), ERG responses were recorded from five mice of each genotype per time point. For scotopic ERG, mice were

A

B

C

D
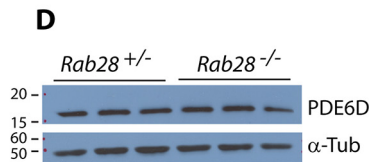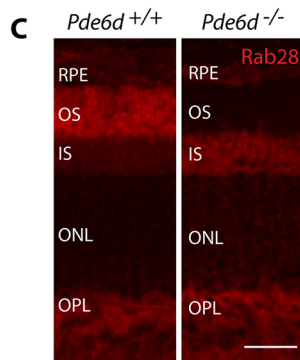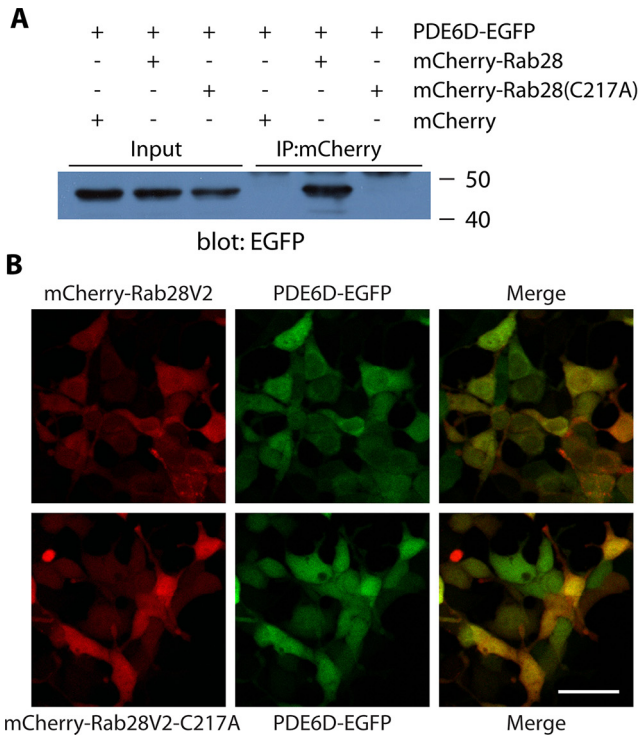
Figure 9. Rab28 interaction with PDE6D is Rab28 prenylation–dependent. *A*, co-IP and Western blotting of PDE6D and RAB28 interaction *in vitro*. PDE6D-EGFP and mCherry-RAB28V2 or mCherry-RAB28V2-C217A were co-expressed in HEK293 cells. Co-IP was performed using monoclonal anti-mCherry antibody or normal mouse IgG, and the blot was probed with anti-EGFP antibody. mCherry-RAB28V2, but not nonfarnesylated mCherry-RAB28V2-C217A, pulls down PDE6D-EGFP. mCherry was used as the co-IP control. *B*, confocal images of proteins expressed *in vitro*. mCherry-RAB28V2 (*red*) and PDE6D-EGFP (*green*) colocalize in the ER and cytoplasm when co-expressed (*top panels*); mCherry-RAB28V2-C217A distributes uniformly throughout the cytoplasm due to the loss of membrane association (*bottom panels*). *C*, WT (*left*) and *PDE6D*$^{-/-}$ (*right*) retina cryosections probed with anti-RAB28 antibody. RAB28 fails to enter the *Pde6d*$^{-/-}$ OS and accumulates primarily in the IS. *D*, immunoblot of *Rab28*$^{+/-}$ and *Rab28*$^{-/-}$ retina homogenates probed with antibodies directed against PDE6D and α-tubulin; PDE6D is not down-regulated in *Rab28*$^{-/-}$ retinas. *Scale bars*, 40 μm (*B*) and 20 μm (*C*).

tested at intensities ranging from −1.63 to 2.38 log cd s/m². For photopic ERG, a rod saturating background light of 1.3979 log cd s/m² was applied for 20 min before and during recording at −0.01 to 1.86 log cd s/m². Bactitracin ophthalmic ointment (Perrigo, Minneapolis, MN) was routinely applied to the eye to prevent infection after ERG testing, and animals were kept on heating pads until fully recovered before being returned to cages. Peak amplitudes for both a- and b-waves were used for analysis using a one-way ANOVA test.
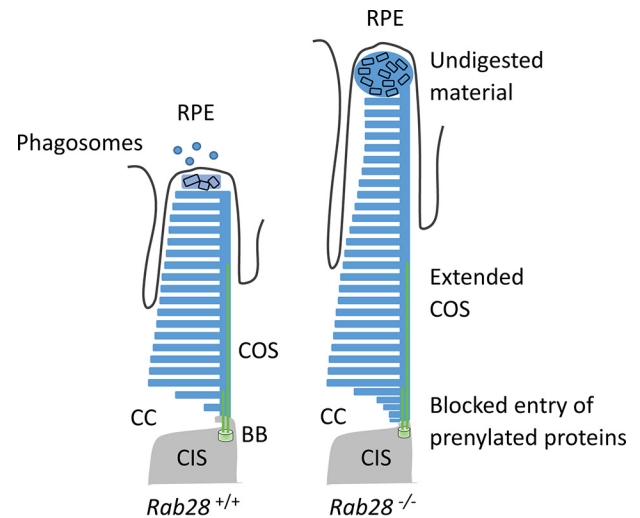
Figure 10. Model of COS disc shedding failure in *Rab28*$^{-/-}$ mouse retina. In WT retina (*left*), COS length is maintained by the daily addition of new disc membranes at the proximal COS and shedding of aged discs at the distal tip. Shed discs are phagocytized by RPE processes. In *Rab28*$^{-/-}$ (*right*), COS shedding at the distal tip fails, elongating COS toward the RPE and accumulating membrane material. Membrane incorporation at the base continues, jamming the ciliary gate and blocking the entry of prenylated proteins. *CC*, connecting cilium; *BB*, basal body; *CIS*, cone inner segment.

Measurement of ONL thickness and OS length

Average ONL thickness and OS length were measured based on DAPI and anti-GC1 antibody fluorescence (48). Cone density was measured based on cone arrestin staining, and COS length was measured based on CNGA3 staining.

In situ phagosome counting

Retina sections collected at 1.5 h after light onset were stained with anti-rhodopsin antibody or mixed anti-ML-opsin and S-opsin antibodies. Rhodopsin-positive phagosomes were counted as described (35). Cone opsin–positive phagosomes were counted from entire retina sections.

Immunofluorescence and confocal microscopy

Staining of cryosections with antibodies and confocal imaging were performed as described (49) with minor modifications. Eyecups were fixed by immersion in ice-cold 4% paraformaldehyde, cryoprotected in 30% sucrose, and embedded in OCT compound. Sections (12 μm thick) were cut using a Micron cryostat and mounted on charged Superfrost® Plus slides (Fisher). Sections were washed in 0.1 M PBS, blocked using 10% normal goat serum or 2% BSA, 0.3% Triton X-100 in PBS, and incubated with primary antibodies at 4 °C overnight. After washes in PBS, signals were detected with Cy3-conjugated or Alexa 488 – conjugated goat anti-rabbit/mouse and/or donkey anti-goat/rabbit/mouse secondary antibody (Jackson ImmunoResearch, Inc.) and counterstained with 1 μl/ml DAPI (Invitrogen). Primary antibodies were as follows: goat anti-RAB28 (Biorbyt), mouse monoclonal anti-rhodopsin (1D4; 1:1000), anti-ROM-1 (1:25) (Dr. Robert Molday, University of British Columbia), anti-GC1 (IS4; 1:1000; Dr. Kris Palczewski, Case Western Reserve University), cyclic nucleotide– gated channel α 1 and 3 (CNGA1/A3) (1:1000; NeuroMab, University of California, Davis, CA), GRK1 (G8, Santa Cruz Biotechnology, Inc.;

SASBMB

J. Biol. Chem. (2018) 293(45) 17546–17558 **17555**

1:300); rabbit polyclonal anti-ML- and S-opsin (Chemicon; 1:1500), CNGA3 (1:500; Dr. Xi-Qin Ding, University of Oklahoma), cTγ (Cytosignal; 1:500), cone arrestin (mCAR; 1:500) (50), PDE6 (MOE, Cytosignal; 1:1500), rod transducin α (Cytosignal; 1:500), and cone PDE6α′ (Dr. Tiansen Li, NEI, National Institutes of Health; 1:40,000). Images were captured using a Zeiss LSM-800 confocal microscope. Some images were adjusted for brightness and contrast using Adobe Photoshop CS3.

Retina protein extraction and Western blotting

Retinas from WT and $Rab28^{-/-}$ mice or bovine were homogenized in radioimmune precipitation assay buffer (10 mM Tris-Cl, pH 8.0, 140 mM NaCl, 1% Triton X-100, 0.1% sodium deoxycholate, 0.1% SDS, 1 mM EDTA, 1 mM phenylmethylsulfonyl fluoride) and centrifuged (13,000 × g, 4 °C, for 20 min), and supernatants were collected. Protein samples were separated by 10–12% SDS-PAGE, transferred to polyvinylidene difluoride membrane, and probed with primary antibodies followed by horseradish peroxidase–conjugated secondary antibody. Antigens were visualized using an ECL-plus kit (Pierce).

RAB28 co-immunoprecipitation

Bovine retinas ($n = 5$) were pooled and homogenized in 50 ml of lysis buffer (50 mM Tris-Cl, pH 7.6, 120 mM NaCl, 0.5% IGEPAL CA-630, 1 mM phenylmethylsulfonyl fluoride, 1× protease inhibitor) using a Dounce homogenizer. Cell debris was removed by centrifugation at 3000 × g, 4 °C, for 5 min. The cleaned samples were centrifuged at 20,000 × g, 4 °C, for 30 min, and the supernatants were collected. The supernatants were precleared with 500 μl of 50% protein G–Sepharose 4 fast flow beads (GE Healthcare) for 30 min. Precleared lysates were divided into 10 aliquots (5 ml each). Half of the aliquots were each incubated with goat anti-RAB28 primary antibody (10 μg), and the other half were incubated with normal goat IgG (10 μg) for 1 h 45 min at 4 °C with gentle agitation, followed by incubation with protein G–Sepharose beads for 45 min. Beads were collected by centrifugation at 2300 × g for 1 min and washed six times in lysis buffer without protease inhibitors and once in 1× PBS. Immunoprecipitated proteins were eluted using an improved soft elution method, which minimally co-elutes immunoglobulin (51). The eluted proteins (200 μl) were incubated with 1 ml of acetone at −20 °C overnight, precipitated by centrifugation at 10,000 × g for 10 min at 4 °C, washed with 75% ethanol, and air-dried. Samples were subjected to quantitative MS.

Quantitative MS

Protein samples were subjected to in-solution tryptic cleavage, as described previously (52). LC-MS/MS analysis was performed using an Ultimate3000 nano-RSLC system (Thermo Scientific) coupled to an Orbitrap Fusion Tribrid mass spectrometer (Thermo Scientific) by a nanospray ion source. Tryptic peptide mixtures were injected automatically and loaded at a flow rate of 30 μl/min in 0.1% TFA in HPLC grade water onto a nano trap column (300-μm inner diameter × 5-mm precolumn, packed with Acclaim PepMap100 C18, 5 μm, 100 Å; Thermo Scientific). After 3 min, peptides were eluted and sep-

arated on the analytical column (75-μm inner diameter × 25 cm, Acclaim PepMap RSLC C18, 2 μm, 100 Å; Thermo Scientific) by a linear gradient from 2 to 30% of buffer B (80% acetonitrile and 0.08% formic acid in HPLC-grade water) in buffer A (2% acetonitrile and 0.1% formic acid in HPLC-grade water) at a flow rate of 300 nl/min over 85 min. Remaining peptides were eluted by a short gradient from 30 to 95% buffer B in 5 min. Analysis of the eluted peptides was performed by an LTQ Fusion mass spectrometer. From the high-resolution MS prescan at a resolution of 120,000 with a mass range of 335–1500, the most intense peptide ions were selected for fragment analysis if they were at least doubly charged. The normalized collision energy for higher-energy collisional dissociation was set to a value of 30, and the resulting fragments were detected in the ion trap. The lock mass option was activated; the background signal with a mass of 445.12003 was used as lock mass (53). Every ion selected for fragmentation was excluded for 20 s by dynamic exclusion. MS/MS data were analyzed using the MaxQuant software (version 1.5.2.8) (54). As digesting enzyme, trypsin/P was selected with maximal 2 missed cleavages. Cysteine carbamidomethylation was set for fixed modifications, and oxidation of methionine and N-terminal acetylation were specified as variable modifications. The data were analyzed by label-free quantification with a minimum ratio count of 2. The first search peptide tolerance was set to 20, the main search peptide tolerance was set to 4.5 ppm, and the requantify option was selected. For peptide and protein identification, the *Bos taurus* subset of the Uniprot database (Release 2013_09) was used, and contaminants were detected using the MaxQuant contaminant search. A minimum peptide number of 2 and a minimum length of 7 amino acids was tolerated. Unique and razor peptides were used for quantification. The match between run options was enabled with a match time window of 0.7 min and an alignment time window of 20 min. The statistical analysis, including ratio, *t* test, and significance calculation, was done using the Perseus software (55).

HEK293 cell culture and transfection

HEK293 cells (ATCC) were grown in Dulbecco's modified Eagle's medium supplemented with 10% fetal bovine serum, 1× penicillin/streptomycin in a standard CO_2 incubator. Cells were transfected with plasmid DNA using Lipofectamine 2000 (Invitrogen) according to the manufacturer's instructions. Two days following transfection, cells were fixed and imaged for protein localization, lysed in radioimmune precipitation assay buffer for Western blotting, or lysed in co-IP lysis buffer (see above) for co-IP experiments.

RAB28V2 neonatal electroporation

For retina electroporation, 0.3 μl (1.5 μg) of pmCherry-RAB28V2 plasmid DNA was electroporated into the right eye subretinal space of P0 WT mice (56). Protein localization was analyzed at P21.

Transmission EM

1- and 2.5-month-old WT and $Rab28^{-/-}$ retinas were fixed 2 h in fixative (2% glutaraldehyde, 1% paraformaldehyde in 0.1 M sodium cacodylate buffer, pH 7.4) at 4 °C, post-fixed for 1 h in

1% osmium tetroxide, and stained *en bloc* with uranyl acetate. Washed specimens were dehydrated through an ascending series of methanol, dried in propylene oxide, and infiltrated overnight with Epon resin mix/propylene oxide (1:1) mixture, followed by 100% Epon resin for 2 days. Specimens were embedded in plastic, and the plastic was cured by incubation in a 60 °C oven for 2 days. Blocks were trimmed, and 1-μm-thick sections were cut to identify and orient photoreceptors near the optic nerve. Ultrathin sections at 60 nm were cut, placed onto slot grids with carbon-coated Formvar film (EMS, Hatfield, PA), post-stained with uranyl acetate followed by lead citrate, and finally examined using a JOEL electron microscope at 75 kV.

Statistics

Data are presented as mean $\pm$ S.D., where *n* represents the number of mice analyzed (ERG, retina measurement, phagosome count), or experiment repeats (RAB28 co-IP). Statistical comparisons (significance level set at $p < 0.05$) were performed using one-way ANOVA for all experimental data.

References

1. Young, R. W. (1967) The renewal of photoreceptor cell outer segments. *J. Cell Biol.* **33**, 61–72 CrossRef Medline

2. Young, R. W., and Bok, D. (1969) Participation of the retinal pigment epithelium in the rod outer segment renewal process. *J. Cell Biol.* **42**, 392–403 CrossRef Medline

3. LaVail, M. M. (1976) Rod outer segment disk shedding in rat retina: relationship to cyclic lighting. *Science* **194**, 1071–1074 CrossRef Medline

4. Steinberg, R. H. (1974) Phagocytosis by pigment epithelium of human retinal cones. *Nature* **252**, 305–307 CrossRef Medline

5. Anderson, D. H., Fisher, S. K., Erickson, P. A., and Tabor, G. A. (1980) Rod and cone disc shedding in the rhesus monkey retina: a quantitative study. *Exp. Eye Res.* **30**, 559–574 CrossRef Medline

6. Long, K. O., Fisher, S. K., Fariss, R. N., and Anderson, D. H. (1986) Disc shedding and autophagy in the cone-dominant ground squirrel retina. *Exp. Eye Res.* **43**, 193–205 CrossRef Medline

7. Fisher, S. K., Pfeffer, B. A., and Anderson, D. H. (1983) Both rod and cone disc shedding are related to light onset in the cat. *Invest. Ophthalmol. Vis. Sci.* **24**, 844–856 Medline

8. Kocaoglu, O. P., Liu, Z., Zhang, F., Kurokawa, K., Jonnal, R. S., and Miller, D. T. (2016) Photoreceptor disc shedding in the living human eye. *Biomed. Opt. Express* **7**, 4554–4568 CrossRef Medline

9. Ruggiero, L., Connor, M. P., Chen, J., Langen, R., and Finnemann, S. C. (2012) Diurnal, localized exposure of phosphatidylserine by rod outer segment tips in wild-type but not Itgb5$^{-/-}$ or Mfge8$^{-/-}$ mouse retina. *Proc. Natl. Acad. Sci. U.S.A.* **109**, 8145–8148 CrossRef Medline

10. Finnemann, S. C., Bonilha, V. L., Marmorstein, A. D., and Rodriguez-Boulan, E. (1997) Phagocytosis of rod outer segments by retinal pigment epithelial cells requires alpha(v)beta5 integrin for binding but not for internalization. *Proc. Natl. Acad. Sci. U.S.A.* **94**, 12932–12937 CrossRef Medline

11. D'Cruz, P. M., Yasumura, D., Weir, J., Matthes, M. T., Abderrahim, H., LaVail, M. M., and Vollrath, D. (2000) Mutation of the receptor tyrosine kinase gene Mertk in the retinal dystrophic RCS rat. *Hum. Mol. Genet.* **9**, 645–651 CrossRef Medline

12. Ryeom, S. W., Sparrow, J. R., and Silverstein, R. L. (1996) CD36 participates in the phagocytosis of rod outer segments by retinal pigment epithelium. *J. Cell Sci.* **109**, 387–395 Medline

13. Carter-Dawson, L. D., and LaVail, M. M. (1979) Rods and cones in the mouse retina. I. Structural analysis using light and electron microscopy. *J. Comp. Neurol.* **188**, 245–262 CrossRef Medline

14. Seixas, E., Barros, M., Seabra, M. C., and Barral, D. C. (2013) Rab and Arf proteins in genetic diseases. *Traffic* **14**, 871–885 CrossRef Medline

15. Shelby, S. J., Feathers, K. L., Ganios, A. M., Jia, L., Miller, J. M., and Thompson, D. A. (2015) MERTK signaling in the retinal pigment epithelium regulates the tyrosine phosphorylation of GDP dissociation inhibitor alpha from the GDI/CHM family of RAB GTPase effectors. *Exp. Eye Res.* **140**, 28–40 CrossRef Medline

16. Donnelly, P., Menet, H., Fouanon, C., Herbert, O., Moisan, J. P., Le Roux, M. G., and Pascal, O. (1994) Missense mutation in the choroideremia gene. *Hum. Mol. Genet.* **3**, 1017 CrossRef Medline

17. Tolmachova, T., Ramalho, J. S., Anant, J. S., Schultz, R. A., Huxley, C. M., and Seabra, M. C. (1999) Cloning, mapping and characterization of the human RAB27A gene. *Gene* **239**, 109–116 CrossRef Medline

18. Brauers, A., Schürmann, A., Massmann, S., Mühl-Zürbes, P., Becker, W., Kainulainen, H., Lie, C., and Joost, H. G. (1996) Alternative mRNA splicing of the novel GTPase Rab28 generates isoforms with different C-termini. *Eur. J. Biochem.* **237**, 833–840 CrossRef Medline

19. Lee, S. H., Baek, K., and Dominguez, R. (2008) Large nucleotide-dependent conformational change in Rab28. *FEBS Lett.* **582**, 4107–4111 CrossRef Medline

20. Roosing, S., Rohrschneider, K., Beryozkin, A., Sharon, D., Weisschuh, N., Staller, J., Kohl, S., Zelinger, L., Peters, T. A., Neveling, K., Strom, T. M., European Retinal Disease Consortium, van den Born, L. I., Hoyng, C. B., Klaver, C. C., et al. (2013) Mutations in RAB28, encoding a farnesylated small GTPase, are associated with autosomal-recessive cone-rod dystrophy. *Am. J. Hum. Genet.* **93**, 110–117 CrossRef Medline

21. Riveiro-Álvarez, R., Xie, Y. A., López-Martínez, M. Á., Gambin, T., Pérez-Carro, R., Ávila-Fernández, A., López-Molina, M. I., Zernant, J., Jhangiani, S., Muzny, D., Yuan, B., Boerwinkle, E., Gibbs, R., Lupski, J. R., Ayuso, C., and Allikmets, R. (2015) New mutations in the RAB28 gene in 2 Spanish families with cone-rod dystrophy. *JAMA Ophthalmol.* **133**, 133–139 CrossRef Medline

22. Lee, G. I., Lee, C., Subramanian, S., Kim, N. K. D., Ki, C. S., Park, W. Y., Kim, B. J., and Kim, S. J. (2017) A novel likely pathogenic variant in the RAB28 gene in a Korean patient with cone-rod dystrophy. *Ophthalmic Genet.* **38**, 587–589 CrossRef Medline

23. Mears, A. J., Kondo, M., Swain, P. K., Takada, Y., Bush, R. A., Saunders, T. L., Sieving, P. A., and Swaroop, A. (2001) Nrl is required for rod photoreceptor development. *Nat. Genet.* **29**, 447–452 CrossRef Medline

24. Mustafi, D., Kevany, B. M., Genoud, C., Okano, K., Cideciyan, A. V., Sumaroka, A., Roman, A. J., Jacobson, S. G., Engel, A., Adams, M. D., and Palczewski, K. (2011) Defective photoreceptor phagocytosis in a mouse model of enhanced S-cone syndrome causes progressive retinal degeneration. *FASEB J.* **25**, 3157–3176 CrossRef Medline

25. Humbert, M. C., Weihbrecht, K., Searby, C. C., Li, Y., Pope, R. M., Sheffield, V. C., and Seo, S. (2012) ARL13B, PDE6D, and CEP164 form a functional network for INPP5E ciliary targeting. *Proc. Natl. Acad. Sci. U.S.A.* **109**, 19691–19696 CrossRef Medline

26. Sergouniotis, P. I., Davidson, A. E., Mackay, D. S., Li, Z., Yang, X., Plagnol, V., Moore, A. T., and Webster, A. R. (2011) Recessive mutations in KCNJ13, encoding an inwardly rectifying potassium channel subunit,

ASBMB

J. Biol. Chem. (2018) 293(45) 17546–17558 **17557**

cause Leber congenital amaurosis. *Am. J. Hum. Genet.* **89,** 183–190 CrossRef Medline

27. Omori, Y., Kitamura, T., Yoshida, S., Kuwahara, R., Chaya, T., Irie, S., and Furukawa, T. (2015) Mef2d is essential for the maturation and integrity of retinal photoreceptor and bipolar cells. *Genes Cells* **20,** 408–426 CrossRef Medline

28. Aït-Ali, N., Fridlich, R., Millet-Puel, G., Clérin, E., Delalande, F., Jaillard, C., Blond, F., Perrocheau, L., Reichman, S., Byrne, L. C., Olivier-Bandini, A., Bellalou, J., Moyse, E., Bouillaud, F., Nicol, X., *et al.* (2015) Rod-derived cone viability factor promotes cone survival by stimulating aerobic glycolysis. *Cell* **161,** 817–832 CrossRef Medline

29. Kusaka, S., Inanobe, A., Fujita, A., Makino, Y., Tanemoto, M., Matsushita, K., Tano, Y., and Kurachi, Y. (2001) Functional Kir7.1 channels localized at the root of apical processes in rat retinal pigment epithelium. *J. Physiol.* **531,** 27–36 CrossRef Medline

30. Zhang, H., Li, S., Doan, T., Rieke, F., Detwiler, P. B., Frederick, J. M., and Baehr, W. (2007) Deletion of PrBP/δ impedes transport of GRK1 and PDE6 catalytic subunits to photoreceptor outer segments. *Proc. Natl. Acad. Sci. U.S.A.* **104,** 8857–8862 CrossRef Medline

31. Lumb, J. H., Leung, K. F., Dubois, K. N., and Field, M. C. (2011) Rab28 function in trypanosomes: interactions with retromer and ESCRT pathways. *J. Cell Sci.* **124,** 3771–3783 CrossRef Medline

32. Jiang, J., Qi, Y. X., Zhang, P., Gu, W. T., Yan, Z. Q., Shen, B. R., Yao, Q. P., Kong, H., Chien, S., and Jiang, Z. L. (2013) Involvement of Rab28 in NF-κB nuclear transport in endothelial cells. *PLoS One* **8,** e56076 CrossRef Medline

33. Zhou, Z., Menzel, F., Benninghoff, T., Chadt, A., Du, C., Holman, G. D., and Al-Hasani, H. (2017) Rab28 is a TBC1D1/TBC1D4 substrate involved in GLUT4 trafficking. *FEBS Lett.* **591,** 88–96 CrossRef Medline

34. Jensen, V. L., Carter, S., Sanders, A. A., Li, C., Kennedy, J., Timbers, T. A., Cai, J., Scheidel, N., Kennedy, B. N., Morin, R. D., Leroux, M. R., and Blacque, O. E. (2016) Whole-organism developmental expression profiling identifies RAB-28 as a novel ciliary GTPase associated with the BBSome and intraflagellar transport. *PLoS Genet.* **12,** e1006469 CrossRef Medline

35. Nandrot, E. F., Anand, M., Almeida, D., Atabai, K., Sheppard, D., and Finnemann, S. C. (2007) Essential role for MFG-E8 as ligand for αvβ5 integrin in diurnal retinal phagocytosis. *Proc. Natl. Acad. Sci. U.S.A.* **104,** 12005–12010 CrossRef Medline

36. Gal, A., Li, Y., Thompson, D. A., Weir, J., Orth, U., Jacobson, S. G., Apfelstedt-Sylla, E., and Vollrath, D. (2000) Mutations in MERTK, the human orthologue of the RCS rat retinal dystrophy gene, cause retinitis pigmentosa. *Nat. Genet.* **26,** 270–271 CrossRef Medline

37. Hall, M. O., Prieto, A. L., Obin, M. S., Abrams, T. A., Burgess, B. L., Heeb, M. J., and Agnew, B. J. (2001) Outer segment phagocytosis by cultured retinal pigment epithelial cells requires Gas6. *Exp. Eye Res.* **73,** 509–520 CrossRef Medline

38. Prasad, D., Rothlin, C. V., Burrola, P., Burstyn-Cohen, T., Lu, Q., Garcia de Frutos, P., and Lemke, G. (2006) TAM receptor function in the retinal pigment epithelium. *Mol. Cell Neurosci.* **33,** 96–108 CrossRef Medline

39. Steinberg, R. H., Wood, I., and Hogan, M. J. (1977) Pigment epithelial ensheathment and phagocytosis of extrafoveal cones in human retina. *Philos. Trans. R. Soc. Lond. B Biol. Sci.* **277,** 459–474 CrossRef Medline

40. Audo, I., Mohand-Said, S., Boulanger-Scemama, E., Zanlonghi, X., Condroyer, C., Démontant, V., Boyard, F., Antonio, A., Méjécase, C., El Shamieh, S., Sahel, J. A., and Zeitz, C. (2018) MERTK mutation update in inherited retinal diseases. *Hum. Mutat.* **39,** 887–913 CrossRef Medline

41. Zhong, H., Chen, Y., Li, Y., Chen, R., and Mardon, G. (2015) CRISPR-engineered mosaicism rapidly reveals that loss of Kcnj13 function in mice mimics human disease phenotypes. *Sci. Rep.* **5,** 8366 CrossRef Medline

42. Hanke-Gogokhia, C., Wu, Z., Gerstner, C. D., Frederick, J. M., Zhang, H., and Baehr, W. (2016) Arf-like protein 3 (ARL3) regulates protein trafficking and ciliogenesis in mouse photoreceptors. *J. Biol. Chem.* **291,** 7142–7155 CrossRef Medline

43. Thomas, S., Wright, K. J., Le Corre, S., Micalizzi, A., Romani, M., Abhyankar, A., Saada, J., Perrault, I., Amiel, J., Litzler, J., Filhol, E., Elkhartoufi, N., Kwong, M., Casanova, J. L., Boddaert, N., *et al.* (2014) A homozygous PDE6D mutation in Joubert syndrome impairs targeting of farnesylated INPP5E protein to the primary cilium. *Hum. Mutat.* **35,** 137–146 CrossRef Medline

44. Mattapallil, M. J., Wawrousek, E. F., Chan, C. C., Zhao, H., Roychoudhury, J., Ferguson, T. A., and Caspi, R. R. (2012) The Rd8 mutation of the Crb1 gene is present in vendor lines of C57BL/6N mice and embryonic stem cells and confounds ocular induced mutant phenotypes. *Invest. Ophthalmol. Vis. Sci.* **53,** 2921–2927 CrossRef Medline

45. Wu, S., Ying, G., Wu, Q., and Capecchi, M. R. (2008) A protocol for constructing gene targeting vectors: generating knockout mice for the cadherin family and beyond. *Nat. Protoc.* **3,** 1056–1076 CrossRef Medline

46. Truett, G. E., Heeger, P., Mynatt, R. L., Truett, A. A., Walker, J. A., and Warman, M. L. (2000) Preparation of PCR-quality mouse genomic DNA with hot sodium hydroxide and tris (HotSHOT). *BioTechniques* **29,** 52–54 CrossRef Medline

47. Ying, G., Avasthi, P., Irwin, M., Gerstner, C. D., Frederick, J. M., Lucero, M. T., and Baehr, W. (2014) Centrin 2 is required for mouse olfactory ciliary trafficking and development of ependymal cilia planar polarity. *J. Neurosci.* **34,** 6377–6388 CrossRef Medline

48. Coleman, J. A., Zhu, X., Djajadi, H. R., Molday, L. L., Smith, R. S., Libby, R. T., John, S. W., and Molday, R. S. (2014) Phospholipid flippase ATP8A2 is required for normal visual and auditory function and photoreceptor and spiral ganglion cell survival. *J. Cell Sci.* **127,** 1138–1149 CrossRef Medline

49. Ying, G., Gerstner, C. D., Frederick, J. M., Boye, S. L., Hauswirth, W. W., and Baehr, W. (2016) Small GTPases Rab8a and Rab11a are dispensable for rhodopsin transport in mouse photoreceptors. *PLoS One* **11,** e0161236 CrossRef Medline

50. Zhu, X., Li, A., Brown, B., Weiss, E. R., Osawa, S., and Craft, C. M. (2002) Mouse cone arrestin expression pattern: light induced translocation in cone photoreceptors. *Mol. Vis.* **8,** 462–471 Medline

51. Antrobus, R., and Borner, G. H. (2011) Improved elution conditions for native co-immunoprecipitation. *PLoS One* **6,** e18218 CrossRef Medline

52. Gloeckner, C. J., Boldt, K., Schumacher, A., and Ueffing, M. (2009) Tandem affinity purification of protein complexes from mammalian cells by the Strep/FLAG (SF)-TAP tag. *Methods Mol. Biol.* **564,** 359–372 CrossRef Medline

53. Olsen, J. V., de Godoy, L. M., Li, G., Macek, B., Mortensen, P., Pesch, R., Makarov, A., Lange, O., Horning, S., and Mann, M. (2005) Parts per million mass accuracy on an Orbitrap mass spectrometer via lock mass injection into a C-trap. *Mol. Cell. Proteomics* **4,** 2010–2021 CrossRef Medline

54. Cox, J., and Mann, M. (2008) MaxQuant enables high peptide identification rates, individualized p.p.b.-range mass accuracies and proteome-wide protein quantification. *Nat. Biotechnol.* **26,** 1367–1372 CrossRef Medline

55. Tyanova, S., Temu, T., Sinitcyn, P., Carlson, A., Hein, M. Y., Geiger, T., Mann, M., and Cox, J. (2016) The Perseus computational platform for comprehensive analysis of (prote)omics data. *Nat. Methods* **13,** 731–740 CrossRef Medline

56. Matsuda, T., and Cepko, C. L. (2004) Electroporation and RNA interference in the rodent retina *in vivo* and *in vitro. Proc. Natl. Acad. Sci. U.S.A.* **101,** 16–22 CrossRef Medline